Pseudo 3-D Simulation of a Falling Film Microreactor

M. Al-Rawashdeh[1,2],V. Hessel[*,1,2], P. Löb[1] and F. Schönfeld[1]

[1] Institut für Mikrotechnik Mainz GmbH, Carl-Zeiss-Str. 18-20, D-55129 Mainz, Germany
[2] Eindhoven University of Technology (TU/e), Department of Chemical Engineering and Chemistry. Den Dolech 2, P.O.Box 513, 5600 MB Eindhoven, The Netherlands

*Corresponding author: Institut für Mikrotechnik Mainz GmbH, Carl-Zeiss-Str. 18-20, D-55129 Mainz, Germany, hessel@imm-mainz.de

Abstract

Gas-liquid falling film microreactors suggest themselves to carry out fast exothermic and mass transfer limited reactions. Since the major rate limiting steps occur on the liquid side, it is important to account for a realistic liquid film profile within the reactor simulation. In the current study we present a so-called pseudo 3-D computational fluid dynamic (CFD) model. Based on the realistic channel geometry profiles and the liquid menisci we describe the liquid film thicknesses, flow velocities, species transport and reactions. The reactor model was developed and validated experimentally by the absorption of CO_2 in NaOH aqueous solution. This 3-D model allows investigating the effects of channel fabrication precision, gas chamber height and the impact of different channel geometry profiles. The simulations show that the impact of channel fabrication imprecision at the current situation is less than 2%. Gas chamber reduction slightly improves the conversion, and the best reactor performance is achieved when operating with the minimum uniform liquid film thicknesses.

Keywords: Falling Film Microreactor, Microstructured Reactor, Pseudo 3-D Model, Gas-liquid Reaction

1. Introduction

Gravity driven liquid films on flat substrates are prone to decay into droplet or rivulet patterns, while microchannels can prevent film break-up and facilitate very stable liquid films with a thickness typically below 100 µm. Therefore, stable and extremely high liquid based specific interfacial areas (up to 20,000 m^2/m^3) are obtained under well-defined conditions. Because of this extremely large surface to volume ratio falling film microreactors, cf. Figure 1, are ideally suited for fast exothermic and mass transfer limited reactions between immiscible phases[1, 2].

The vital part of the falling film microreactor is the liquid film and in particular the gas-liquid interface where reactions predominantly take place. Generally, the interface shape is governed by the Weber number (kinetic energy of the liquid over the interfacial energy). At low liquid flow rates, which are investigated in the present study, the interface assumes a stationary shape with constant curvature minimizing the interfacial free energy of the system. Moreover, the channel cross section profile is curved which results in spatial varying liquid film thicknesses and distinctive velocity and residence time distributions. By the means of pseudo 3-D simulations, considering realistic channel geometry profile and liquid menisci, we investigate the role of channel fabrication imprecision, gas chamber height and channel geometry profile on the reactor performance.

1.1 Reaction system

The reaction system considered is the absorption of carbon dioxide from a mixture of CO_2-N_2 into an aqueous solution of NaOH. The reaction steps for CO_2 absorption in aqueous solutions of sodium hydroxide are as follows:

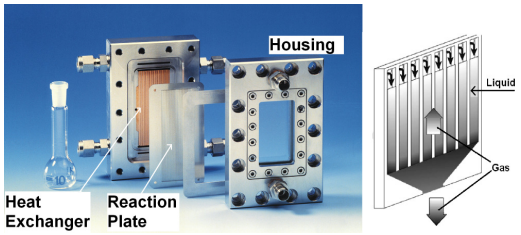

Figure 1. Left: the falling film microreactor main components. Right: schematic view of the structured reaction plate and the continuous contacting between the gas-liquid phases. The grey arrows indicate that the gas flow can be applied in co- or counter-current mode.

$$CO_{2(g)} \Leftrightarrow CO_{2(l)} \quad (1)$$

$$CO_{2(l)} + OH^- \Leftrightarrow HCO_3^- \quad (2)$$

$$HCO_3^- + OH^- \Leftrightarrow CO_3^{2-} + H_2O \quad (3)$$

The overall reaction can be written as

$$2NaOH + CO_2 \Leftrightarrow Na_2CO_3 + H_2O \quad (4)$$

Keeping the pH of the solution above 11 makes sure that all of the CO_2 converts to CO_3^{2-} and the amount of HCO_3^- is negligible[3]. Therefore, reaction (3) is significantly faster than reaction (2). Accordingly, reaction (2), which is governed by second order kinetics, determines the overall rate of reaction $R = k_{OH^-} c_{OH^-} c_{CO_2}$.

1.2 Reaction channels

The microchannels are fabricated via wet chemical etching[4]. Because of the fabrication technique, slight variations in the channel cross section dimensions are observed[5]. Typical etched channel profiles are semi-elliptic as measured by Yeong et al.[6] In order to quantify the deviations between different channel cross-section dimensions, laser-scanning surface profilometry measurements were done at Institut für Mikrotechnik Mainz GmbH (IMM). These measurements were done at 9 different locations distributed over the length and width of a single stainless steel plate equipped with 16 channels with cross sectional dimensions of about 1200 µm x 400 µm and channel length of 6.64 cm. The maximum deviation in the channel width (W) and depth (D) are found to be 46 µm and 21 µm respectively.

1.3 Meniscus shape

Generally, the interface shape is governed by the kinetic energy of the liquid and the interfacial energy, the ratio of which is given by the Weber number. At low liquid flow rates the interface will assume a stationary shape with constant curvature minimizing the interfacial free energy of the system[7]. The operational conditions used in the present study imply a Weber number below 10^{-3}. Hence, the interface is dominated by the surface energy and a stationary, spatially non-varying meniscus with a constant curvature can be assumed, cf. Figure 2.

2. Numerical model

2.1 Momentum balance

In the present approach possible changes of physical properties due to the absorption and

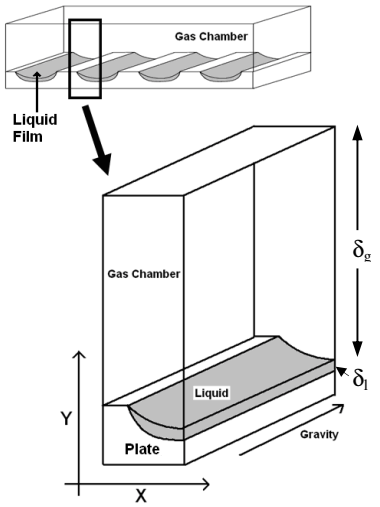

Figure 2. Top: schematic view of the microstructured plate, the liquid volumes (grey) and the gas chamber. Bottom: enlarged view of the geometry part which is considered in the CFD model. The liquid film is characterized by its central height, i.e. the liquid height at the symmetry boundary (δ_l). Also the gas domain is specified by its height, i.e. the distance from the gas–liquid interface to the upper wall (δ_g).

reaction of CO_2 are neglected and a fully developed flow is assumed. In this case the 3-D Navier-Stokes equations, governing the three Cartesian velocity components, reduce to a single 2-D Poisson equation for the cross sectional profile of the axial velocity component. Since the liquid flow is solely driven by gravity, the momentum balance in the liquid domain reads:

$$-\mu_l \left(\frac{\partial^2 v_{l,z}}{\partial x^2} + \frac{\partial^2 v_{l,z}}{\partial y^2} \right) = \rho_l g \ , \quad (5)$$

where μ_l, ρ_l and $v_{l,z}$ denote the dynamic liquid viscosity, density and axial velocity component. At the channel wall the no-slip condition is applied, i.e. $v_{l,z} = 0$. On the gas side the flow is mainly driven by the application of an external pressure, whereas gravity does virtually play no role. In analogy to the liquid side the hydrodynamic equations reduce to a single Poisson equation governing the axial velocity component:

$$-\mu_g \left(\frac{\partial^2 v_{g,z}}{\partial x^2} + \frac{\partial^2 v_{g,z}}{\partial y^2} \right) = \frac{\partial P}{\partial z} \ , \quad (6)$$

where μ_g and $v_{g,z}$ denote the dynamic gas viscosity and axial velocity component. Here no-slip and free-slip (symmetry) boundary conditions apply at the top wall and at the side walls, respectively. The internal boundary conditions at the stationary gas-liquid interface imply continuity in the velocity and shear stress.

2.2 Material balance

Generally, all species Na^+, OH^-, H^+, H_2O, HCO_3^-, CO_3^{2-} and CO_2 in aqueous solution are to be considered in the liquid domain. However, keeping the pH of the solution above 11 makes OH^-, CO_3^{2-} and CO_2 as the only species of interest to perform the material balance in the liquid phase. The gas flow contains N_2 and CO_2, since all other species in the liquid phase are assumed as being nonvolatile. The steady state concentration fields c_i in the liquid as well as in the gas phase are governed by advection-diffusion-reaction equations. If axial diffusion is neglected, the 3-D steady state equation can be transformed into a 2-D transient equation by identifying the time coordinate with the axial coordinate[8]. The transformed material equation in Cartesian coordinates reads

$$v_{l,z}\frac{\partial c_{l,i}}{\partial z} = D_{l,i}\left(\frac{\partial^2 c_{l,i}}{\partial x^2}+\frac{\partial^2 c_{l,i}}{\partial y^2}\right)+R_i \quad , \qquad (7)$$

$$v_{g,z}\frac{\partial c_{g,i}}{\partial z} = D_{g,i}\left(\frac{\partial^2 c_{g,i}}{\partial x^2}+\frac{\partial^2 c_{g,i}}{\partial y^2}\right) , \qquad (8)$$

where D_i, c_i denote the diffusion coefficient, component concentration and the subscripts *l, g* specify the liquid and gas phase, respectively. And R_i is the reaction rate in the liquid phase. Zero flux boundary conditions are applied at the walls and symmetry faces, i.e. $\partial_n c_i = 0$, where ∂_n denotes the derivative in the direction normal to the boundary. The same boundary condition holds for all species, except CO_2 at the gas-liquid interface, since these species are assumed to be confined to their respective phases. The equations governing the species concentrations in the liquid and in the gas phase are coupled by the mass transfer of CO_2 across the interface, which is governed by the equilibrium relation of Henry's law. The concentration in the liquid phase at the interface is given by $c_{l,CO_2\ \text{at interface}} = HP_{CO_2}$, where P_{CO_2} denotes the partial pressure of carbon dioxide in the gas phase and *H* the Henry constant. In the gas phase the boundary condition at the interface is given by mass conservation

$$J_{g,CO_2} = D_{l,CO_2}\left.\frac{\partial c_{l,CO_2}}{\partial y}\right|_{\text{interface}} \qquad (9)$$

where J_{g,CO_2} is the mass flux of CO_2 out of the gas phase. Boundary condition at the inlet translates to an initial condition in the pseudo 3-D approach and reads $c_i = c_{i,0}$. N_2 is calculated as background fluid and the mole fraction (Y) is computed from the amount of CO_2 remaining in the gas phase as $Y_{N_2} = 1 - Y_{CO_2}$.

2.3 Simulation procedure

Comsol Multiphysics (Release 3.3a) in combination with Matlab was used to solve the four PDEs, eqn.5, 6, 7 and 8. Due to the symmetry of the channel cross section only half of it is considered in the model. Figure 2 shows the model geometry and specifies the chosen coordinate system. The measured channel geometry profile was fitted by means of a least-squares method within Origin (OriginLab 7.5G SR6). The fitted channel profile together with the circular meniscus constitutes the liquid domain. A 2-D structured mesh with about 3000 cells was used for spatial discretization of the cross sectional plane. In order to resolve the steep gradients occurring in the species concentrations the mesh was refined close to the gas-liquid interface, yielding minimum cell dimensions of about 0.5 µm. For discretization in the time domain, time steps between 0.01-0.05 s were used.

Within the experiment the meniscus height of the gravity driven liquid film adjusts to the applied flow rate. However, within the present simulation approach the liquid height has to be specified prior to the simulation while setting up the geometry. Therefore, we start by computing a calibration curve solving Eq. 5 for various meniscus heights. We find a reasonably good agreement for the liquid flow rate at a specified liquid height between the respective approach

and the experimental results from Yeong et al[6]. A specific gas flow rate, on the other hand, is applied by simply adjusting the pressure gradient, cf. Eq. 6. Subsequently to the simulation of the fluidic part the velocity fields were applied for the computation of species concentrations. The complete reaction conversion was calculated by integration of respective concentrations over the domain area, which is the X-Y cross sectional area seen in Figure 2.

The molar concentration of NaOH was 1 M, isothermal condition was assumed at 25° C and the total pressure was 1 bar. To maintain NaOH in excess the inlet molar ratio $n_{CO_2,g}/n_{OH^-}$ was set to 0.4. These operation conditions were kept throughout the study, expect where explicitly stated otherwise.

3. Results and Discussion

3.1 Model validation

Model validation was done by comparing simulation with experimental results. The experiment was run at constant liquid flow rate 3.3 ml/min, while the CO_2 mole fraction was varied by changing gas flow rate of N_2. Figure 3 shows that present model results agree well with the experimental data.

3.2 Liquid flow rate variation and fabrication precision

To reveal the effect of microchannel fabrication imprecisions, two channels representing extreme uncertainties in the channel cross-section dimensions were studied. The respective real channel profiles were inserted in the simulation with deviations in width of 46 µm and in depth of 21 µm. By means of the outlined model, reaction conversions at various liquid flow rates, from 1.6 to 20 ml/min, were calculated. For each liquid flow rate the CO_2 mole fraction was kept constant at 10% by adjusting the gas flow rate to have the molar ratio $n_{CO_2,g}/n_{OH^-}$ fixed to 0.4. The result in Figure 4 shows that the CO_2 conversion decreases as the liquid flow rate increases, which can be attributed to the reduction in the residence time. Moreover, it turned out that the difference in CO_2 conversion among both channels is small (about 2%). Further simulation results, not presented here, show that the reaction takes place within a range of only a few micrometers close the gas-liquid interface. However the meniscus interfacial area does only weakly change within the mentioned channels fabrication imprecision. Thus even comparatively large differences in microchannels dimensions due to fabrication imprecision do not lead to a large shift in the reaction conversion. And so the channel fabrication precision at the current situation is satisfactory.

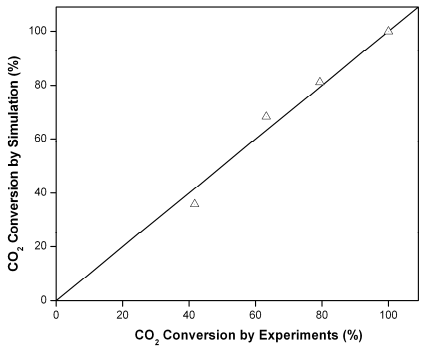

Figure 3. Simulated versus experimental reaction conversions.

3.3 Gas chamber height reduction

Falling film microreactors with different gas chamber heights ranging from 5.5 mm to 0.7 mm were investigated experimentally as well as by simulation. The liquid flow rate was kept constant at 3.3 ml/min. Simulation as well as experimental data are shown in Figure 5.

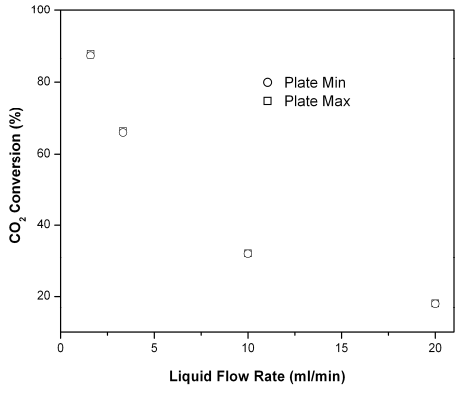

Figure 4. Effect of fabrication precision on the conversion for different flow rates. Channel profiles with the lowest dimension is denoted by Min and the larger channel dimension is denoted by Max.

As to be expected, the results show that the conversion increases with increasing CO_2 mole fraction. Increasing CO_2 mole fraction enhances mass transfer by increasing the driving force. At constant CO_2 mole fraction, the conversion in the experiments is found to be slightly increased by lowering the gas chamber. Narrowing gas chamber height increases the gas velocity and accordingly the residence time is decreased. On the other hand, the CO_2 diffusion time to reach the interface is decreased. The ratio between residence time and diffusion time is given by the Fourier number,

$$Fo = \frac{t_g}{\tau_d} \quad , \qquad (12)$$

where t_g and τ_d are the gas residence time and CO_2 diffusion time to reach the interface, respectively. The experimental data clearly show that larger Fourier numbers are preferable. The simulation results, on the other hand, show a much lower dependency on the gas chamber height than what is observed in the experiments. The differences may be due to the enhancement of the gas phase mass transfer due to the vortex formation[9].

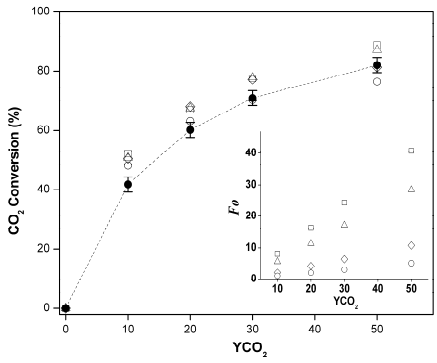

Figure 5. Dependence of the conversion on CO_2 mole fraction and on the gas chamber height. Open symbols denote experimental reaction conversion results as function of CO_2 concentration for four different gas chamber heights; (□) δ_g = 0.70 mm, (Δ) δ_g = 1.00 mm, (◊) δ_g = 2.65 mm, (○) δ_g = 5.5 mm. For the sake of clarity simulation results are shown for one gas chamber height (δ_g = 2.65 mm) only with filled circles. The error bars denote the variation of the simulation results for varying gas chamber heights which is about twice the symbol size. The inset shows corresponding Fourier number (Fo) in the gas phase for different gas chamber heights.

Whereas, in the simulation fully developed uniaxial flow is assumed and only one half of a single fluid channel and the corresponding gas chamber above it are taken into account. Thus the 3-D swirling flow and the resulting 'cross-talk' between individual channels are not considered. As the gas chamber height gets narrower the Reynolds numbers get larger and accordingly the flow of gas can not be described accurately by the present simulation model.

3.4 Microchannel shape

Next, the impact of the microchannel shape on the reactor performance was investigated. To this end five representative channel shapes as shown in Figure 6 have been selected. Both, channel width and central depth are kept constant in this study, *viz.* 1200 µm and 400 µm. In order to evaluate the different shapes, we define an intensification factor as the normalized liquid flow rates over the total structured area necessary to attain a 95% CO_2 conversion,

$$IF = \frac{F_L}{W L_{95\%CO_2} N_{ch}} \qquad (13)$$

Here in the chosen approach, the channel length $L_{95\%CO_2}$ corresponds to the residence time which had been adjusted to achieve the 95% CO_2 conversion. *IF* denotes the intensification factor, *W* is the channel width, N_{ch} the total number of channels in the plate. The intensification factor allows to quantitatively compare different channel shapes at different operating conditions. A high intensification factor corresponds to the ability to achieve 95% conversion at a large liquid flow rates using only a small structured area.

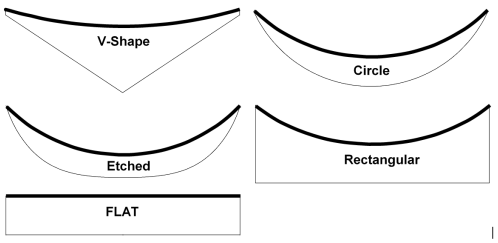

Figure 6. Studied microchannel shapes. Five different channel shapes including the liquid film and meniscus. The bold line denotes the liquid meniscus, i.e. the liquid-gas interface. The thin line represent the channel wall, i.e. liquid-solid interface.

Moreover, the OH^- mass transfer limitation (RM) is calculated. To this end, the diffusion coefficient of OH^- is artificially increased by a factor of 100 within the simulations. Accordingly the OH^- mass transfer rate enhances and the channel length needed to reach 95% CO_2 conversion reduces. Dividing the channel length with artificially increased mass transfer by the actual channel length (the case with actual diffusion), gives a measure for the mass transfer limitation. Note, here we focus on the transport of OH^- ions only, because it has been identified to affect the conversion most when channel geometry changed.

$$RM = \frac{L_{95\%\ CO_2\ \text{conversion},\ 100xD}}{L_{95\%\ CO_2\ \text{conversion},\ D}} \qquad (14)$$

In Figure 7, the results of the intensification factor (see left axis) and the mass transfer limitation (see right axis) at different liquid flow rates are shown for the various channel shapes and liquid flow rates considered.

3.4.1 Flat

The flat geometry represents a hypothetical situation where a flat channel shape and a flat liquid meniscus form the liquid film. As the liquid flow rate decreases the liquid film thickness decreases, while the intensification factor increases, see Figure 7. The reduction in the liquid film thickness reduces the OH^- mass transfer distance, the distance from the microchannel bottom to the gas-liquid interface, where the reaction takes place. Hence, the OH^- mass transfer limitation reduces and RM reaches almost one for the minimum liquid film thickness. Therefore, in the flat microchannel, the best performance can be achieved when operating with the minimum liquid film thickness.

3.4.2 Circle

In contrast to the flat microchannel performance, the worst performance for the circular microchannel achieved for the lowest liquid flow rate, cf. Figure 7. As the liquid flow rate decreases, a spatial varying liquid film thicknesses form, not shown here, causes large variations in the velocity profile, a wider residence time distribution. Therefore a steep OH^- concentration profile is formed and so the OH^- mass transfer limitation increases.

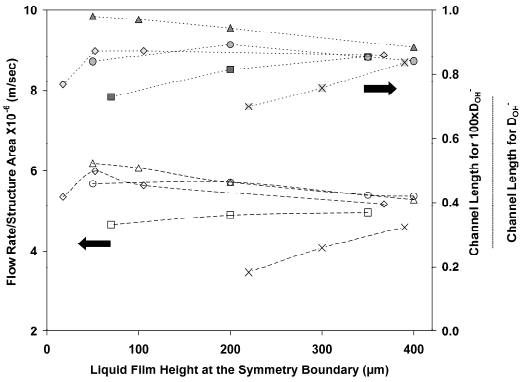

Figure 7. Intensification factor and resistance to mass transfer of OH^- ions at different liquid flow rates and channel shapes, (Δ) Flat, (○) Rectangular, (◊) Etched, (□) Circle, (X) V-shape. Open symbol denote the intensification factors given at the left axis. Filled symbols denote the OH^- resistance to mass transfer given at the right axis.

However, as the liquid flow rate increases the liquid film thicknesses gets more uniform resulting in narrower residence time distribution. This explains the best performance found at the largest liquid flow rate.

3.4.3 V-Shape

Similar to the circular microchannel the V-shape channel shows the best performance at large liquid flow rates. Both microchannel shapes, V-shape and circular shape, have a similar behavior for the liquid film thicknesses and velocity profiles in relation with the liquid flow rate.

3.4.4 Rectangular

The liquid velocity profile in the rectangular channel changes strongly with applied liquid flow rates. At the minimum liquid flow rate two velocity maxima exist which are located near the channel corners[7]. When the liquid flow rate increases the maxima of the velocity profile start shifting to the microchannel center where they finally merge. At larger liquid flow rates the liquid velocity profile looks similar to that of the V-shaped and circular microchannel. Here, the largest intensification factor is found for an optimum liquid flow rate of 34.2 ml/min which correspond to a liquid film height of 200 µm, cf. Figure 7. At the optimum liquid flow rate the uniformity of the spatially liquid film thicknesses in the channel and the shape of the velocity profile result in narrower residence time

distribution. Hence, less steep OH^- concentration profile, and the less resistance to mass transfer.

3.4.5 Etched
The liquid velocity profile in the etched microchannel is very similar to that of the rectangular microchannel. Accordingly, we find the largest value of the intensification factor for specific optimum liquid flow rate of 0.94 ml/min corresponding to liquid film thickness equal to 52.5 µm.

3.4.6 Comparison of all microchannel shapes performance
In conclusion we find that the best channel performance is for the flat geometry while the worst one is for the V-Shape. Moreover, the differences in the performances are found to be strongly related to the mass transport, in particular to the diffusion of OH^- ions. The best channel geometry is to the one with the minimum, spatially uniform liquid film thickness, which is found in the hypothetical case of a flat meniscus. For a real etched geometry profile the best performance was found at an optimum liquid flow rate of 0.94 ml/min corresponding to liquid film thickness equal to 52.5 µm.

4. Conclusions and Outlook
A 3-D elaborated model considering the liquid meniscus and curved channel profiles is developed. This model is validated experimentally by the absorption of CO_2 in a NaOH aqueous solution. Microchannel fabrication precision at the current situation is found to be satisfactory since it is shown to affect the reaction conversion by less than 2%. Beside the reactor characterization, the reactor geometry analysis confirms that a reduction in the gas chamber height slightly improves the conversion and gas phase mass transfer limitations can be overcome. The best reactor performance is reached when operating with the minimum, spatially uniform liquid film thickness. For the etched geometry this corresponds to an optimum flow rate of 0.94 ml/min corresponding to a liquid film thickness of 52.5 µm.
The CFD model facilitates to accurately describe the meniscus shape, hydrodynamic flow field, together with diffusive, advective species transport and reactions. Therefore, it can now be used to identify favorable channel geometries and optimum operating conditions. This paves the ground for the scale-out of the falling film microreactors in order to better and faster transfer the process-intensification achievements to future real-case

8. References

1. Vankayala, B., Löb, P., Hessel, V., Menges, G., Hofmann, C., Metzke, D., Krtschil, U. and Kost, Hans-Joachim, Scale-up of Process Intensifying Falling Film Microreactors to Pilot Production Scale, *International Journal of Chemical Reactor Engineering*, **5**, A91 (2007).
2. Hessel, V., Löwe, H., Müller, A. and Kolb, G. *Chemical Micro Process Engineering*. Wiley-VCH, Weinheim (2005).
3. Fleischer, C., Becker, S. and Eigenberger, G., Detailed modeling of the chemisorption of CO_2 into NaOH in a bubble column, *Chemical Engineering Science*, **51**, 1715-1724 (1996).
4. Hessel, V., Kolb, G. and Brandner, J.. *Microfabrication for Energy Generating Devices and Fuel Processors*, in: Mitsos, A. *Micropower Devices*, Wiley-VCH, Weinheim (to be released in 2008).
5. Nageswara, R. and Deepak, K., *Fabrication of microchannels on stainless steel by wet chemical etching*. Journal of Micromechanics and Microengineering, **17**, N99-N106 (2007).
6. Yeong, K.K., Gavrillidis, A, Zapf, R., Kost, H.J., Hessel, V., Boyde, A. *Characterization of liquid film in a microstructed falling film reactor using laser scanning confocal microscopy*. Experimental Thermal and Fluid Science, **30**, 463-472 (2006).
7. Hardt, S., Doffing, F. and Pennemann, H. *Simulation of hydrodynamic dispersion in gas/liquid microreactors*. Nanotech, **1**. 54-57 (2002).
8. Comsol Multiphysics 3.3a, *User guide of chemical engineering module in Comsol documentation*, pp 157-158 (2007).
9. Commenge, J.M., Obein, T., Genin, G., Framboisier, X., Rode, S., Schanen, V., Pitiot, P. and Matlosz, M. *Gas-phase residence time distribution in falling film microreactor*. Chemical Engineering Science, **61**, 597-604 (2005).